Open Archive Toulouse Archive Ouverte (OATAO)

OATAO is an open access repository that collects the work of Toulouse researchers and makes it freely available over the web where possible

This is an author's version published in: http://oatao.univ-toulouse.fr/25596

Official URL: https://doi.org/10.1002/adfm.201903960

Any correspondence concerning this service should be sent to the repository administrator: tech-oatao@listes-diff.inp-toulouse.fr

3D Macroscopic Architectures from Self-Assembled MXene Hydrogels

Tongxin Shang, Zifeng Lin, Changsheng Qi, Xiaochen Liu, Pei Li, Ying Tao,* Zhitan Wu, Dewang Li, Patrice Simon,* and Quan-Hong Yang*

Assembly of 2D MXene sheets into a 3D macroscopic architecture is highly desirable to overcome the severe restacking problem of 2D MXene sheets and develop MXene-based functional materials. However, unlike graphene, 3D MXene macroassembly directly from the individual 2D sheets is hard to achieve for the intrinsic property of MXene. Here a new gelation method is reported to prepare a 3D structured hydrogel from 2D MXene sheets that is assisted by graphene oxide and a suitable reductant. As a supercapacitor electrode, the hydrogel delivers a superb capacitance up to 370 F g^{-1} at 5 A g^{-1}, and more promisingly, demonstrates an exceptionally high rate performance with the capacitance of 165 F g^{-1} even at 1000 A g^{-1}. More-over, using controllable drying processes, MXene hydrogels are transformed into different monoliths with structures ranging from a loosely organized porous aerogel to a dense solid. As a result, a 3D porous MXene aerogel shows excellent adsorption capacity to simultaneously remove various classes of organic liquids and heavy metal ions while the dense solid has excellent mechanical performance with a high Young's modulus and hardness.

1. Introduction

MXenes, with the formula $M_{n+1}X_nT_x$—where M is a transition metal, X is C and/or N, and T_x denotes surface functionalization—are a new emerging class of 2D materials, which are prepared by selectively etching away the A-group (generally group IIIA and IVA elements) layers from the MAX phases.[1,2] Their unique structure and surface chemistry give MXenes many key properties, such as metallic conductivity (6000–8000 S cm^{-1}),[3] a hydrophilic surface, and good mechanical stability,[4] which distinguish them from other 2D materials and make them promising candidates for energy storage,[5,6] electromagnetic-interference shielding,[3] transparent conductors,[7] catalysis,[8] and sensor[9] applications.

However, similar to other 2D materials, their performance is hindered by their tendency to stack or aggregate, which severely limits their applications in many fields. Strategies including the introduction of interlayer spacers,[5,10–13] creating porous structures,[14,15] and integrating 2D MXene sheets into 3D macroscopic structures have been proposed to tackle those issues.[15–19] Typically, Gogotsi's group reported that Ti_3C_2 intercalated with dimethyl sulfoxide shows excellent Li-ion capacity at extremely high charging rates.[13] It is reported using sacrificial poly(methyl methacrylate) spherical templates to produce 3D macroporous films is another efficient way to increase the MXene surface accessibility.[17] Flexible MXene foams prepared by a hydrazine-induced foaming process from assembled MXene films show excellent electromagnetic-interference shielding.[15] In addition to these efforts of engineering MXene film, 3D MXene-based composites prepared by the ice-template method or Ti_3C_2 hydrogel without volume shrinkage from a high concentration MXene dispersion have been reported recently.[18,19] Unfortunately, the MXene assembly at high concentration solutions would make the restacking or aggregation of MXene sheets worse, which no doubt would adversely affect their surface utilization. Considering the intrinsic property of MXene like the superior hydrophilic nature, the small size, and the rigidity of MXene flakes, it is still a challenge to achieve the direct assembly of individual MXenes sheets into a 3D macrostructure with a stable interlinked network.

T. X. Shang, C. S. Qi, X. C. Liu, P. Li, Prof. Y. Tao, Z. T. Wu,
D. W. Li, Prof. Q.-H. Yang
Nanoyang Group
State Key Laboratory of Chemical Engineering
School of Chemical Engineering and Technology
Tianjin University
Tianjin 300350, China
E-mail: yingtao@tju.edu.cn; qhyangcn@tju.edu.cn
T. X. Shang, C. S. Qi, X. C. Liu, P. Li, Prof. Y. Tao, Z. T. Wu,
D. W. Li, Prof. Q.-H. Yang
Collaborative Innovation Center of Chemical Science
and Engineering (Tianjin)
Tianjin 300350, China
Prof. Z. F. Lin
College of Materials Science and Engineering
Sichuan University
Chengdu 610065, China
Prof. P. Simon
CIRIMAT
Université de Toulouse
CNRS
INPT
UPS 118 route de Narbonne, Toulouse 31062, France
E-mail: simon@chimie.ups-tlse.fr

Here we report the formation of a 3D MXene hydrogel (denoted as MXH) by a self-assembly approach in the presence of graphene oxide (GO) and ethylenediamine (EDA). When used as a supercapacitor electrode, the 3D hydrogel achieves a superb gravimetric capacitance and rate performance as a result of the rapid electron transfer and ion transport to redox-active sites in the porous 3D MXene macroassembly. With dif-ferent drying processes, MXene hydrogels are transformed into MXene monoliths (MXMs) with entirely different morpholo-gies and microstructures, either as loosely organized aerogels or densely structured xerogels, which is similar to those for graphene hydrogels.[20] The porous 3D MXene foam (F-MXM) through freeze-drying shows a high adsorption performance for the removal of various classes of organic liquids and heavy metal ions, while the capillary induced dense 3D MXene mon-olith (D-MXM) has a high Young's modulus and hardness, demonstrating their potential use in environmental cleaning, mechanics, and energy storage.

2. Results and Discussion

The MXH can be easily prepared from a homogeneous MXene aqueous dispersion (2–10 mg mL^{-1}) containing 5–20 wt% GO and a trace of EDA in a sealed glass vial at 95 °C for 6 h (**Figure 1**). The formation of MXH can be clearly seen in Video S1 in the Sup-porting Information. Similar to EDA-promoted GO gelation,[21,22] the assembly of MXene is proposed to occur as follows: i) ring opening of epoxy groups attached to GO layers is initiated by EDA to form oxygen dangling bonds, and the MXene flakes then react with these bonds to form hybrid structures of MXene and par-tially reduced GO (rGO) and ii) the formation of the MXH is then driven by van der Waals forces and π–π stacking interactions of the hybrid nanosheets. In this way, the MXH can be easily manu-factured on a large-scale (Figure S1, Supporting Information). As shown in **Figure** 2a-c, the MXH has a well-defined and intercon-nected 3D porous network as shown in the scanning electron microscope (SEM) images of its freeze-dried samples (F-MXM). The pore size of the network ranges from sub-micrometers to several micrometers and the pore walls consist of stacked MXene flakes crosslinked by rGO sheets. A very stiff material with an obvious volume shrinkage and dense microstructure (D-MXM) is obtained when capillary-drying is used to remove the water from the hydrogel (Figure 2d–f). Nitrogen adsorption–desorption isotherms and pore size distributions of the MXene powder, F-MXM, and D-MXM are shown in Figure 2g,h. The D-MXM

has a high specific surface area of 196 m^2 g^{-1} compared to the reported MXene-based materials, whose surface areas range from ≈10 to 30 m^2 g^{-1}.[11,14]

As observed from the SEM, transmission electron micro-scope (TEM), and atomic force microscope (AFM) images of the MXene sheets (Figure S2, Supporting Information), it has a 2D lamellar structure without obvious wrinkles, which indi-cates that the MXene sheets are not as flexible as graphene. MXene sheets and large graphene sheets form a hybrid scaf-fold as shown in TEM images of hybrid sheets at different magnifications (**Figure** 3a,b) and energy dispersive X-ray spec-trum (EDS) elemental maps of the two components (Figure 3c). The crosslinked MXene and rGO sheets are more flexible and thicker and are wrinkled. The elemental maps in Figure 3c show uniform distributions of Ti, C, O, N, and F elements in the F-MXM. In Figure 3d, the (002) diffraction peak shifts from 7.1° for MXene powder to 6.5° for F-MXM after the introduction of the rGO, corresponding to an increased inter-layer spacing from 1.18 to 1.37 nm. There is no characteristic TiO_2 peak in the X-ray diffraction (XRD) pattern of F-MXM, indicating crosslinking of the MXene sheets by the functional groups of the GO layers rather than oxidation of the MXene sheets. The Raman spectra (Figure S3, Supporting Informa-tion) of MXene powder and F-MXM are similar in the range of 100 to 750 cm^{-1}, but two broad bands indicating the presence of graphene appear at 1320 and 1595 cm^{-1} for F-MXM, which confirms the incorporation of MXene and rGO sheets.

To investigate the effect of GO, we used different amounts of GO in the assembly of MXene (Figure 3e). All the hydro-gels prepared with different amounts of GO have a smooth surface with differential volume shrinkage, which is an impor-tant indicator for the formation of the stable 3D interconnected frameworks. Nevertheless, with a decrease of the amount of GO in the MXene system, a more expanded hydrogel is obtained because of the lower crosslinking index. A MXene hydrogel cannot be obtained without the addition of GO. We found that GO is crucial to construct the 3D macrostructures. To further investigate the mechanism of MXH formation, high-resolution X-ray photoelectron spectroscopy (XPS) spectra of the Ti 2p (**Figure** 4a), O 1s (Figure S4b, Supporting Information) and C 1s (Figure S4c, Supporting Information) of MXene powder and F-MXM were recorded. The Ti 2p core level peak can be fitted by a contribution of three doublets (Ti 2p$_{3/2}$–Ti 2p$_{1/2}$), in agree-ment with other reports.[12,23] The Ti 2p core level peak contri-butions for F-MXM and MXene powder were determined using the nonlinear least square method. As shown in Figure 4a,
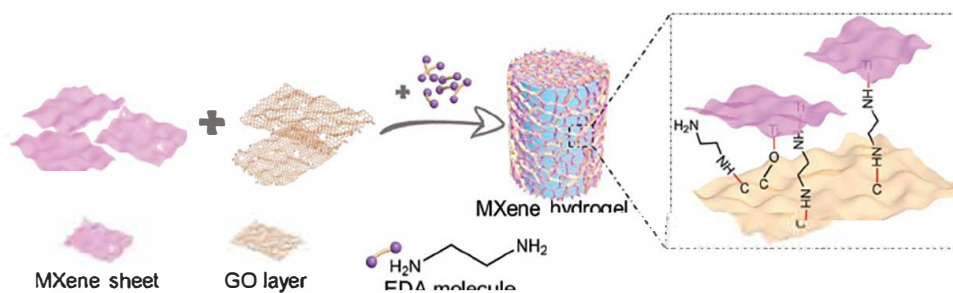

Figure 1. Schematic illustration of the formation process of MXene hydrogel.
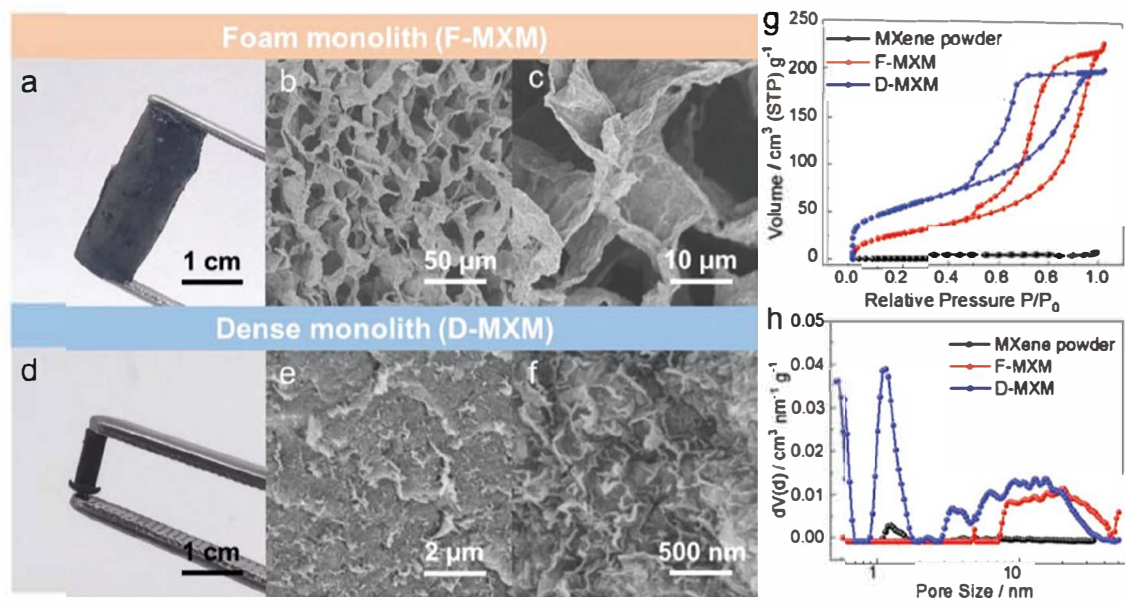
Figure 2. The morphology and microstructure of MXM: Optical photographs and SEM images at different magnifications of the MXH with a–c) freeze-drying and d–f) capillary-drying. g) Nitrogen adsorption/desorption isotherms and h) pore size distributions of MXene powder and MXMs.

the Ti—O oxide peak (458.5 eV) was well resolved for F-MXM, indicating the oxidation of the MXene sheets by the functional groups of the GO layers.[12,24] The atomic percentage of Ti-O (531.8 eV) in all fitted components increased from 40.6% for MXene powder to 50.3% for F-MXM, also confirming the

interaction between the MXene layers and the GO sheets at sites of oxygen dangling bonds (Figure S4b, Supporting Information).[19,22,25] The Ti-O (458.5 and 531.8 eV) peak is ascribed to the formation of TiO_2. However, the XRD pattern shows no characteristic peaks for TiO_2, and the Raman spectrum of
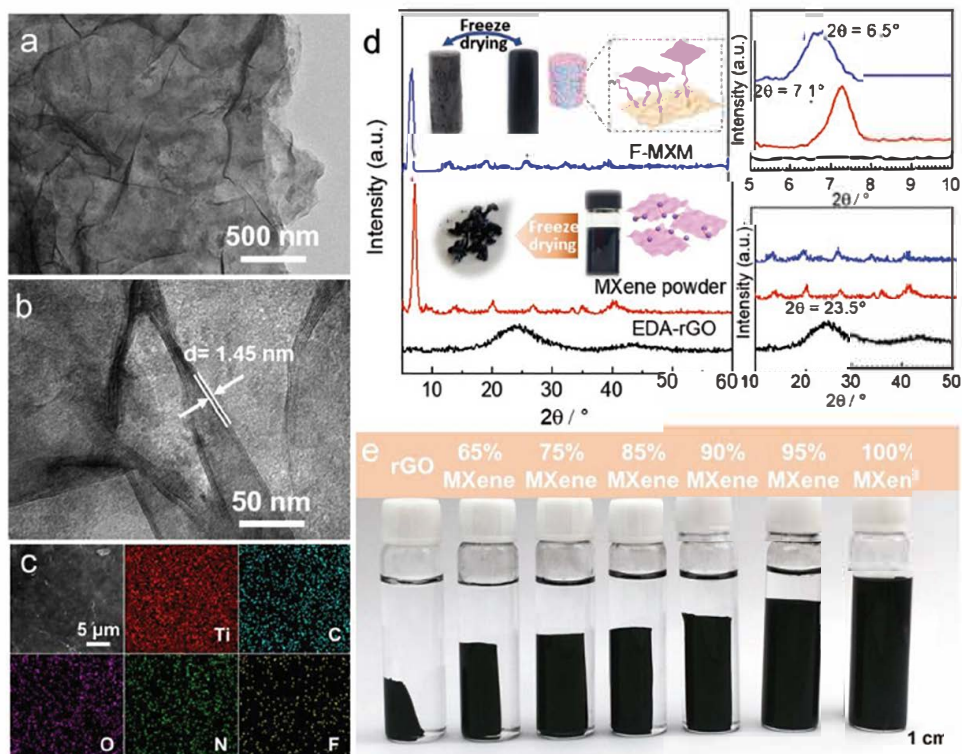

Figure 3. Characterization of MXH and F-MXM: a,b) TEM images of MXH at different magnifications. c) SEM image and corresponding EDS elemental maps of Ti, C, O, N, and F in F-MXM. d) XRD patterns of EDA-rGO, MXene powder, and F-MXM. e) Optical photographs of the hydrogels prepared with different amounts of graphene oxide.
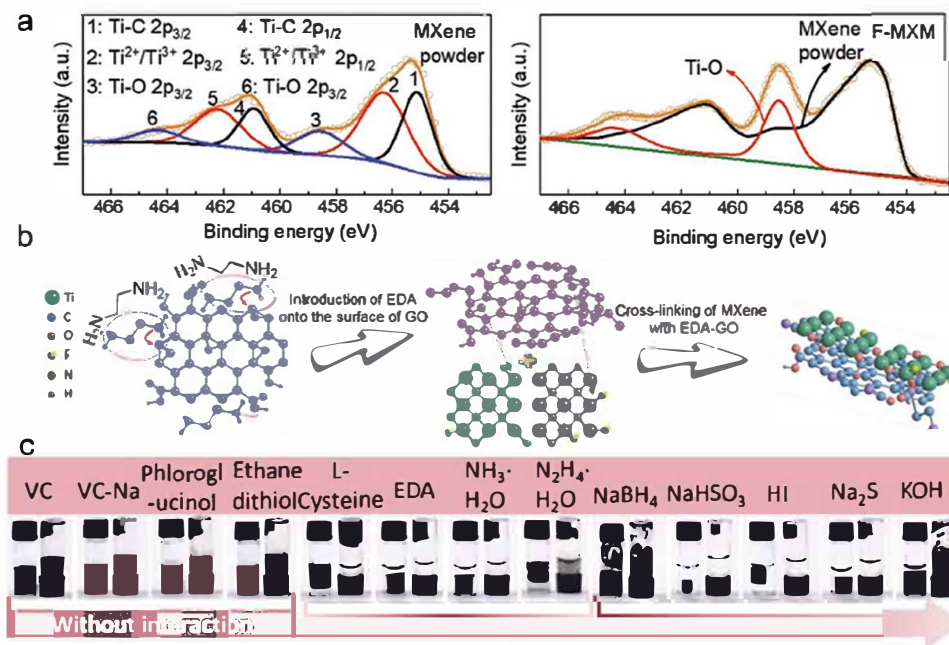
Figure 4. Mechanisms proposed for the assembly of MXene: a) Ti 2p spectra of MXene powder and F-MXM. b) Formation mechanism of MXH. c) Photographs of the hydrogels prepared with different reductants.

F-MXM shows similar vibrations in the Raman shift range $100–750$ cm^{-1}, suggesting that the increase of the Ti-O oxide peak mainly comes from the crosslinking of MXene and GO. Meanwhile, the F 1s XPS spectrum of F-MXM is almost unobservable (Figure S4a, Supporting Information), which indicates that the formation of the Ti–O bond is due to O substitution of the F atom in Ti–F bonds. Such an interaction between MXene and GO sheets is supposed to be the fundamental for the crosslinking of these two 2D nanosheets and formation of MXH (the reaction pathway is shown in Figure 4b). The C 1s core level was fitted with six components centered at 281.8, 282.5, 284.8, 285.1, 286.2, and 288.3 eV, which were assigned to C–Ti, C–Ti–O, C–C, C–N, C–O, and O=C–O bonds, respectively. In F-MXM, the increased number of C–O bonds confirms the interaction between MXene and rGO sheets, and a slight decrease in the number of C–O bonds for F-MXM-95% compares with that for F-MXM-90% (Table S1, Supporting Information). As shown in Table S1 in the Supporting Information, the number of C–N bonds decreases as the amount of GO used decrease. This shows that the introduction of EDA onto the surface of the GO layers and the reaction of EDA with hydroxyl/epoxy groups is located on GO sheets.[21]

Besides, the MXene hydrogel cannot form in the mixture solution of GO/MXene free of EDA (Figure S5a, Supporting Information). Only oxidized MXene precipitate and rGO hydrogel were obtained due to the reduction of GO by MXene, which can be identified from the Fourier transform infrared spectroscopy (FTIR) (Figure S5b, Supporting Information). Those results indicate that these two components fail to crosslink with each other in the absence of EDA. In addition, control experiments were performed by assembling MXene solely with GO using a hydrothermal process (free of EDA). As shown in Figure S6a in the Supporting Information, the two com-

ponents have no effective interaction with each other, leading to obvious delamination. There is only a limited effect on the formation of MXH when the EDA content decreases from 50 to 1 wt% as shown in Figure S6b in the Supporting Information. However, nanosheet aggregates begin to form when the EDA content is decreased to 0.5 wt% and these aggregates are unable to assemble into a hydrogel (Figure S6c, Supporting Information) because the mixed nanosheets are not stable in a neutral aqueous solution. Besides, the selection of reductant will significantly affect the assembly process of MXene and GO. As shown in Figure 4c, L-cysteine, ammonium hydroxide (NH$_3$·H$_2$O), hydrazine hydrate (N$_2$H$_4$·H$_2$O), sodium hydrogen sulfite (NaHSO$_3$), hydroiodic acid, and sodium sulfide (Na$_2$S) all show a similar effect to EDA because the ring-opening of epoxy groups attached to the GO layers is initiated by these reductants via nucleophilic reactions to form oxygen dangling bonds,[25–27] which are available for the crosslinking of most of the MXene flakes and the rGO sheets. For a strong reductant (sodium borohydride (NaBH$_4$)) or a weak reductant (potassium hydroxide (KOH)), a broken or structure unstable MXH is obtained because of the excessive or inadequate reduction. However, other reductants without an amino group and a different reduction mechanism cannot take part in the crosslinking process. For L-ascorbic acid sodium salts, phloroglucinol, ethanedithiol, etc., carboxyl groups will be removed preferentially instead of oxygen dangling bonds being formed by oxygen ring-opening.[25,28] As a result, a rGO hydrogel will be obtained rather than an MXH, so that both GO and EDA (or similar reductants) are needed for the formation of MXH. EDA provides the crosslinking sites for the MXene flakes and the partially reduced GO sheets. The inherent flexibility of the rGO sheets is crucial for neutralizing the rigidity of the MXene flakes and building the 3D macrostructures. Then the assembly
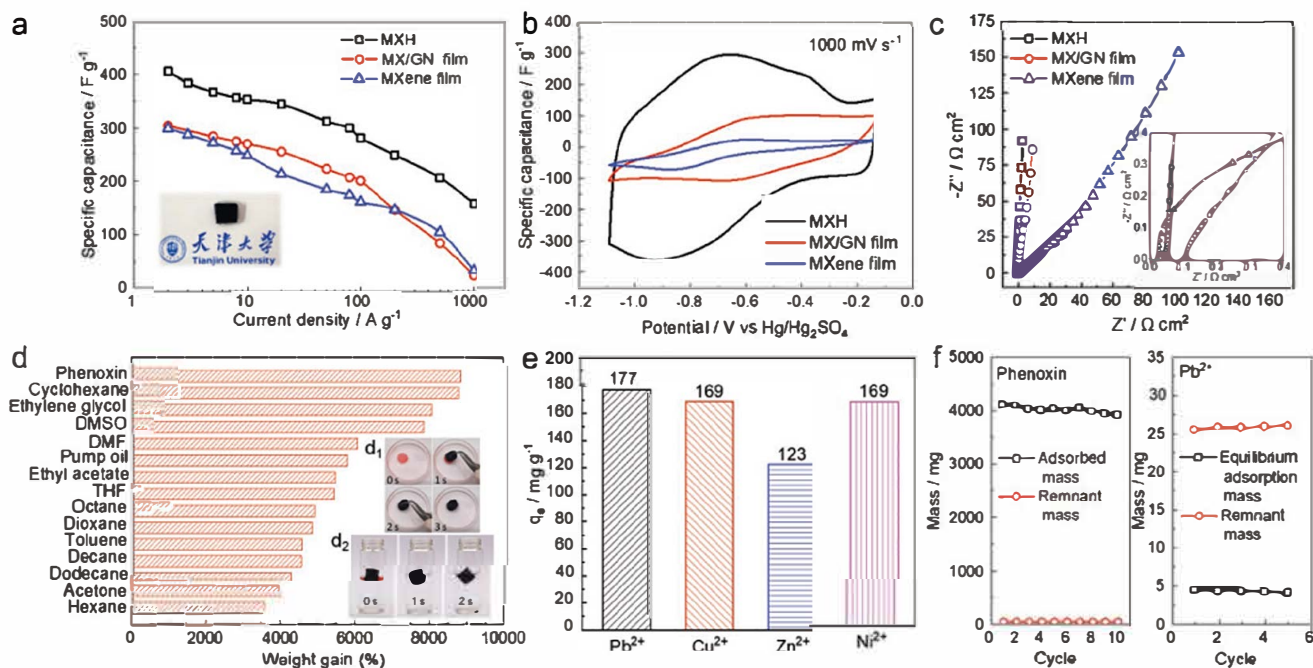
Figure 5. Electrochemical and adsorption performance of the MXH and F-MXM electrodes: a–c) Electrochemical performance of the MXH, MX/GN film, and MXene film electrodes: a) rate performance at current densities ranging from 0.2 to 1000 A g^{-1}, b) cyclic voltammetry profiles collected at 1000 mV s^{-1} and c) Nyquist plots collected at open circuit potential. d) Absorption efficiency of F-MXM in terms of weight gain (inset: d$_1$) adsorption of phenoxin and d$_2$) dodecane in F-MXM at intervals of 2–3 s). e) Adsorption capacity of several heavy metal ions on F-MXM. f) Absorption recyclability of F-MXM for phenoxin and Pb^{2+}.

of MXene flakes are driven by the van der Waals force between the MXene flakes and assisted by the π–π interaction of rGO sheets crosslinked with MXene. Hence, the as-prepared MXHs are structurally stable and mechanically strong, which can be further confirmed by rheological tests (Figure S7, Supporting Information). The viscosity of the MXH decreased greatly as it was sheared, which is typical of an assembled hydrogel and similar to a self-assembled graphene hydrogel.[29] The storage and loss modulus of these materials are better those of conventional self-assembled hydrogels[30–32] and are comparable to those of various chemically crosslinked polymer hydrogels and some biological tissues,[33,34] both in a small-deformation oscillatory measurement and in a thermal stability test.

The sliced MXH can be directly used as the supercapacitor electrodes without a binding agent and/or conducting additive because of their high porosity and conductivity, and excellent mechanical strength. The 3D MXH electrode showed a dramatic increase in capacitance and rate performance over the 2D hybrid film of MXene and reduced graphene oxide (MX/GN film) and MXene film electrodes (**Figure** 5a–c and Figure S8, Supporting Information). Specifically, the 3D MXH electrodes have an ultrahigh gravimetric capacitance of 370 F g^{-1} at 5 A g^{-1} with a potential window of 0.95 V, which is among the highest values reported for MXene-based materials with such a wide potential window.[11,12,35–38] At the same time, the 3D MXH electrodes showed an exceptionally high rate handling ability for a pseudocapacitive materials, with gravimetric capacitance of 165 F g^{-1} even at 1000 A g^{-1} (Figure 5a). The capacitance of the MXH electrodes at high scan rates is still superior to values obtained using a vertically aligned liquid-crystal

MXene electrode[37] and a macroporous Ti$_3$C$_2$T$_x$ electrode[38] (Figure S8c, Supporting Information), in sharp contrast to the pronounced increased internal resistance drop at 1000 A g^{-1} (Figure S8b, Supporting Information) and the polarization at 1000 mV s^{-1} (Figure 5b) for the MX/GN film and MXene film electrodes. The MXene-based supercapacitors show an excellent cycle performance, retaining over 98% of their capacitance after 10 000 cycles at a high scan rate of 1000 mV s^{-1} (Figure S8d, Supporting Information). To shed light on the charge storage kinetics, b value was calculated according to $i_p = av^b$, and close to 1 even at a scan rate of 5000 mV s^{-1} for MXH electrodes, demonstrating an excellent capacitive storage behavior (Figure S8e, Supporting Information). A steeper slope of the Nyquist plot in the low frequency range for the MXH electrode indicates that the 3D architectures provide a smooth and convenient ion-transport path, as well as delivering macroporosity and low pore tortuosity (Figure 5c). Overall, the 3D assembly is beneficial for a high rate transfer and ion transport to redox-active sites, ensuring the excellent electrochemical performance of the supercapacitor.

To further explore and understand possible applications, the MXHs were dried using different processes and MXene monoliths in foam (F-MXM) or dense (D-MXM) forms with different pore size distributions were obtained. Interestingly, the pore structure of the 3D MXene material can be tuned using the different drying processes; as a result, two monoliths with a macroporous and a microporous structure and distinct densities (0.027 and 2.1 g cm^{-3}, respectively) could be easily prepared. For the foam monolith, its properties, including pore structure, surface functionalization and mechanical

stability, make it a promising adsorbing material for removing oils or other organic pollutants. As shown in Figure 5d, it has an excellent adsorption capacity for different organic liquids including common pollutants and organic solvents. F-MXM can adsorb an amount of liquid up to 30–90 times its own weight, which is much higher than other similar sorbents such as a hydrazine-treated MXene film (2.9–32 times),[15] boron nitride (BN) (16–46 times),[39] etc. and compares with some carbon foams[40,41] (Figure S9 and Table S2, Supporting Information). In particular, a maximum weight gain of 8700% for phenoxin was achieved relative to the weight of the F-MXM. The insert in Figure 5d shows the efficient absorption of phenoxin (Figure 5d$_1$) and dodecane (Figure 5d$_2$) with a series of photos (the adsorbates were stained with Sudan red 5B). In this series 1 g dodecane on water is absorbed completely by a 19.6 mg F-MXM within 2 s (Figure 5d$_2$), indicating an average absorption rate of 21.05 g per gram of F-MXM per second (g g^{-1} s^{-1}) which is much faster than many graphene foams ($\approx$0.57 g g^{-1} s^{-1}).[40] F-MXM has a two-efficiency adsorption capacity for oils/organic pollutants and heavy metal ions. A series of batch tests of its adsorption of toxic heavy metal ions was performed using the bottle-point methods shown in Figure 5e. Pb(II), Cu(II), Zn(II), and Ni(II) were selected as model toxic metals because of their high toxicity and carcinogenicity and because they are listed as a priority heavy metal pollutants by most national environmental protection agencies. The adsorption performance and mechanism of Pb(II) onto MXene (Ti$_3$C$_2$T$_x$) phase was revealed by Peng's group,[42] but our results further endorse the potential use of MXene-based materials in environmental cleanup because of their 3D macroscopic architectures. At room temperature, adsorption capacities of 177, 169, 123, and 169 mg g^{-1} for Pb(II), Cu(II), Zn(II), and Ni(II), respectively, could be achieved. These results reveal that F-MXM has larger sorption capacities for many kinds of heavy metals compared to other heavy metal ion adsorbents (Table S3, Supporting Information). Because of the simplicity of the assembly of MXene, a high accessible surface area and the large number of active sites available in the 3D framework greatly improve the adsorption capacity for various heavy metal ions. In contrast, although the carbon foam had a high adsorption capacity for various classes of organic liquids, its adsorption capacity for heavy metal ions was very low as was the specific surface area. The absorption recyclability of F-MXM for phenoxin and Pb^{2+} was tested and results are shown in Figure 5f. The process was repeated ten times for phenoxin to check the feasibility and completeness of recycling organics from F-MXM, followed by the regeneration of F-MXM by releasing the phenoxin in ethanol and drying. Less than 0.5% of the residual weight of adsorbates remained in the F-MXM after each cycle, indicating its highly stable recycling performance. For the desorption of Pb^{2+}, the adsorption efficiency reached 85% and the adsorption capacity remained at 165 mg g^{-1} in each cycle. It is important to note that F-MXM could be used as a dual-function sorbent because of its 3D porous structure and abundant hydroxyl groups which provided some ion-change sites by cation substitution. As shown in Figure S10a in the Supporting Information, D-MXM exhibits a similar adsorption capacity toward heavy metal ions to that of F-MXM. Besides, D-MXM shows superior mechanical properties as measured by a Hysitron nanoindenter equipped with a Berkovich tip (Figure S10, Supporting Information). An average of ten measurements at various sites gave Young's modulus and hardness values of 15 and 0.7 GPa which are higher than those of carbon-based monoliths such as graphene/carbon nanotubes (6.5 and 0.18),[43] 3D nanographene (0.3–1 and 0.02–0.1),[44] graphene oxide composites (1.1 and 1.2×10^{-3}),[45] 3D graphene foam (1.2×10^{-3}–1.5×10^{-3} and 9.1×10^{-5}–2.6×10^{-5})[46] etc. The Young's modulus was also tested by a resonant ultrasound spectrometer (UMS-100) and a similar result (12.8 GPa) was obtained. The D-MXM with good mechanical properties and strongly bonded nanoconstituents has the potential for use in numerous applications, such as nano-microelectromechanical systems, sensors, dampers, etc.

3. Conclusion

In conclusion, we have demonstrated the preparation of 3D MXene monoliths by the gelation of MXene in solution in the presence of GO and EDA. GO acts as a crosslinking agent, and during the gelation, EDA initiates the ring-opening of epoxy groups present on the GO layers and the oxygen dangling bonds formed react with the MXene flakes to form the hydrogel. When used as an electrode the 3D hydrogel achieves superb gravimetric capacitance and rate performance because of the high electron transfer rate and the fast ion transport toward redox-active sites in the MXene macroassembly with a 3D porous structure. The hydrogel has also been transformed into mechanically strong and thermally stable 3D monoliths with different porous structures, and these have emerged as an important class of functional materials and have received increasing interest from the scientific community. Typically, the as-prepared foam-like porous monolith shows interesting adsorption properties for the removal of organic liquids and heavy metal ions while the dense solid monolith has excellent mechanical performance with a high Young's modulus and hardness. This work is important for the promotion of the large-scale use of MXene-based functional materials and gives new insight into the better design and preparation of materials assembled from 2D nanosheets.

4. Experimental Section

Synthesis of Ti$_3$C$_2$T$_x$ and GO: A mixture of hydrochloric acid (HCl) and lithium fluoride (LiF) was used to synthesize multilayer Ti$_3$C$_2$T$_x$ from Ti$_3$AlC$_2$.[38] Specifically, 2 g LiF was added to 40 mL 9 M HCl, followed by the slow addition of 2 g Ti$_3$AlC$_2$ in an ice bath. After etching for 24 h at 35 °C, the multilayer Ti$_3$C$_2$T$_x$ was washed and centrifuged with deionized water until the supernatant reached a pH value of $\approx$6. Next, a delaminated Ti$_3$C$_2$T$_x$ colloidal solution was prepared by sonication for 1 h with bubbling Ar gas protection. After the mixture was centrifuged for 1 h at 3500 rpm to eliminate the sediment, a colloidal suspension of few-layer Ti$_3$C$_2$T$_x$ was obtained in the dark supernatant. Graphite oxide was prepared from graphite powder using a modified Hummers' method as reported earlier.[47] A GO colloidal suspension (2 mg mL^{-1}) was prepared by ultrasonication of GO in water for 2 h, followed by mild centrifugation (3800 rpm for 20 min) to remove thick layers.

Preparation of MXene Hydrogels: Typically, colloidal suspension of Ti$_3$C$_2$T$_x$ (10 mg mL^{-1}) and appropriate amounts of the GO colloidal suspension (2 mg mL^{-1}) were mixed and then sonicated for about

20 min to obtain a homogeneous solution, while bubbling Ar gas through the mixture. The mass fraction of GO was about 10 wt% and 25 µL EDA was added per 10 mL of the mixed solution. It was then sealed in a glass vial and heated for 6 h at 95 °C for the assembly of the MXene hydrogel. The as-formed hydrogel was immersed in deionized water and washed for several times until the pH of the water adjacent to the hydrogel approximate neutrality to remove residual EDA. After freeze-drying or capillary evaporation-induced drying, MXene monoliths with different pore structures and densities were obtained and marked as a foam-like monolith or a dense monolith. For comparison, the MXene solution with EDA was heated under the same conditions and an MXene powder was obtained after freeze-drying. A 2D hybrid film of MXene and reduced graphene oxide (MX/GN film) was prepared for comparison by vacuum-filtration with the same weight proportion of MXene and rGO as in MXH.

Characterization and Measurements: The morphology and pore structure of samples were characterized by a SEM (Hitachi S-4800, 3 kV), a TEM (JEM 3100F), and an automated surface area and pore size analyzer (Belsorp-Mini, N_2, 77 K). Other characterizations were made by XRD (Bruker D-8), XPS (Thermo ESCALAB 250Xi equipped with monochromatic Al K_α source of 1486.5 eV), Raman spectroscopy (Renishaw-inVia Raman spectroscope with an excitation at 532 nm), and versatile automated AFM-Raman NTEGRA Spectra (NT-MDT). The rheological behavior of the MXene hydrogels was investigated by an MCR 301 rheometer using 25 mm parallel-plate geometry at 25 °C. The gap distance between the two plates was fixed to be 2 mm.

Electrochemical Measurements: All electrochemical tests were performed using an Eco Chemie Autolab 128N electrochemical workstation (Metrohm, Switzerland) equipped with an FRA2 frequency response analyzer module and Nova software. Galvanostatic charge/discharge and cyclic voltammetry measurements were conducted in three-electrode stainless steel Swagelok cells. A MXene-based electrode on a glassy carbon current collector was used as the working electrode and over-capacitive activated carbon was used as the counter electrode. The reference electrode was Hg/Hg_2SO_4 in a saturated K_2SO_4 solution. The same three-electrode cell configuration described above was used for electrochemical impedance spectroscopy in the 10 mHz to 100 kHz range using a potential amplitude of 5 mV.

Supporting Information

Supporting Information is available from the Wiley Online Library or from the author.

Conflict of Interest

The authors declare no conflict of interest.

[1] B. Anasori, Y. Xie, M. Beidaghi, J. Lu, B. C. Hosler, L. Hultman, P. R. C. Kent, Y. Gogotsi, M. W. Barsoum, *ACS Nano* **2015**, *9*, 9507.

[2] M. Naguib, O. Mashtalir, J. Carle, V. Presser, J. Lu, L. Hultman, Y. Gogotsi, M. W. Barsoum, *ACS Nano* **2012**, *6*, 1322.

[3] F. Shahzad, M. Alhabeb, C. B. Hatter, B. Anasori, S. Man Hong, C. M. Koo, Y. Gogotsi, *Science* **2016**, *353*, 1137.

[4] M. Naguib, V. N. Mochalin, M. W. Barsoum, Y. Gogotsi, *Adv. Mater.* **2014**, *26*, 992.

[5] M. R. Lukatskaya, O. Mashtalir, C. E. Ren, Y. Dall'Agnese, P. Rozier, P. L. Taberna, M. Naguib, P. Simon, M. W. Barsoum, Y. Gogotsi, *Science* **2013**, *341*, 1502.

[6] B. Anasori, M. R. Lukatskaya, Y. Gogotsi, *Nat. Rev. Mater.* **2017**, *2*, 16098.

[7] A. D. Dillon, M. J. Ghidiu, A. L. Krick, J. Griggs, S. J. May, Y. Gogotsi, M. W. Barsoum, A. T. Fafarman, *Adv. Funct. Mater.* **2016**, *26*, 4162.

[8] J. Ran, G. Gao, F.-T. Li, T.-Y. Ma, A. Du, S.-Z. Qiao, *Nat. Commun.* **2017**, *8*, 13907.

[9] S. J. Kim, H.-J. Koh, C. E. Ren, O. Kwon, K. Maleski, S.-Y. Cho, B. Anasori, C.-K. Kim, Y.-K. Choi, J. Kim, Y. Gogotsi, H.-T. Jung, *ACS Nano* **2018**, *12*, 986.

[10] M. Boota, B. Anasori, C. Voigt, M. Q. Zhao, M. W. Barsoum, Y. Gogotsi, *Adv. Mater.* **2016**, *28*, 1517.

[11] J. Li, X. Yuan, C. Lin, Y. Yang, L. Xu, X. Du, J. Xie, J. Lin, J. Sun, *Adv. Energy Mater.* **2017**, *7*, 1602725.

[12] J. Yan, C. E. Ren, K. Maleski, C. B. Hatter, B. Anasori, P. Urbankowski, A. Sarycheva, Y. Gogotsi, *Adv. Funct. Mater.* **2017**, *27*, 1701264.

[13] O. Mashtalir, M. Naguib, V. N. Mochalin, Y. Dall'Agnese, M. Heon, M. W. Barsoum, Y. Gogotsi, *Nat. Commun.* **2013**, *4*, 1716.

[14] P. Lian, Y. Dong, Z.-S. Wu, S. Zheng, X. Wang, S. Wang, C. Sun, J. Qin, X. Shi, X. Bao, *Nano Energy* **2017**, *40*, 1.

[15] J. Liu, H.-B. Zhang, R. Sun, Y. Liu, Z. Liu, A. Zhou, Z.-Z. Yu, *Adv. Mater.* **2017**, *29*, 1702367.

[16] Y. Ma, Y. Yue, H. Zhang, F. Cheng, W. Zhao, J. Rao, S. Luo, J. Wang, X. Jiang, Z. Liu, N. Liu, Y. Gao, *ACS Nano* **2018**, *12*, 3209.

[17] M.-Q. Zhao, X. Xie, C. E. Ren, T. Makaryan, B. Anasori, G. Wang, Y. Gogotsi, *Adv. Mater.* **2017**, *29*, 1702410.

[18] Y. Yue, N. Liu, Y. Ma, S. Wang, W. Liu, C. Luo, H. Zhang, F. Cheng, J. Rao, X. Hu, J. Su, Y. Gao, *ACS Nano* **2018**, *12*, 4224.

[19] L. Li, M. Zhang, X. Zhang, Z Zhang, *J. Power Sources* **2017**, *364*, 234.

[20] Y. Tao, X. Xie, W. Lv, D.-M. Tang, D. Kong, Z. Huang, H. Nishihara, T. Ishii, B. Li, D. Golberg, F. Kang, T. Kyotani, Q.-H. Yang, *Sci. Rep.* **2013**, *3*, 2975.

[21] J. Che, L. Shen, Y. Xiao, *J. Mater. Chem.* **2010**, *20*, 1722.

[22] S. Stankovich, D. A. Dikin, R. D. Piner, K. A. Kohlhaas, A. Kleinhammes, Y. Jia, Y. Wu, S. B. T. Nguyen, R. S. Ruoff, *Carbon* **2007**, *45*, 1558.

[23] M. Hu, T. Hu, Z. Li, Y. Yang, R. Cheng, J. Yang, C. Cui, X. Wang, *ACS Nano* **2018**, *12*, 3578.

[24] Q. Yang, Z. Xu, B. Fang, T. Huang, S. Cai, H. Chen, Y. Liu, K. Gopalsamy, W. Gao, C. Gao, *J. Mater. Chem. A* **2017**, *5*, 22113.

[25] X. Gao, J. Jang, S. Nagase, *J. Phys. Chem. C* **2010**, *114*, 832.

[26] W. Chen, L. Yan, P. R. Bangal, *J. Phys. Chem. C* **2010**, *114*, 19885.

[27] C. K. Chua, M. Pumera, *Chem. Soc. Rev.* **2014**, *43*, 291.

[28] M. J. Fernández-Merino, L. Guardia, J. I. Paredes, S. Villar-Rodil, P. Solís-Fernández, A. Martínez-Alonso, J. M. D. Tascón, *J. Phys. Chem. C* **2010**, *114*, 6426.

[29] C. L. Yuxi Xu, K. Sheng, G. Shi, *ACS Nano* **2010**, *4*, 4324.

[30] R. Xing, S. Li, N. Zhang, G. Shen, H. Möhwald, X. Yan, *Biomacro-molecules* **2017**, *18*, 3514.

[31] L. Jiang, D. Xu, T. J. Sellati, H. Dong, *Nanoscale* **2015**, *7*, 19160.

[32] C. Karavasili, A. Komnenou, O. L. Katsamenis, G. Charalampidou, E. Kofidou, D. Andreadis, S. Koutsopoulos, D. G. Fatouros, *ACS Biomater. Sci. Eng.* **2017**, *3*, 3386.

[33] O. Chaudhuri, L. Gu, D. Klumpers, M. Darnell, S. A. Bencherif, J. C. Weaver, N. Huebsch, H. P. Lee, E. Lippens, G. N. Duda, D. J. Mooney, *Nat. Mater.* **2016**, *15*, 326.

[34] C. Qiao, X. Ma, J. Zhang, J. Yao, *Food Chem.* **2017**, *235*, 45.

[35] C. Yang, Y. Tang, Y. Tian, Y. Luo, M. Faraz Ud Din, X. Yin, W. Que, *Adv. Energy Mater.* **2018**, *8*, 1802087.

[36] Y. Yoon, M. Lee, S. K. Kim, G. Bae, W. Song, S. Myung, J. Lim, S. S. Lee, T. Zyung, K.-S. An, *Adv. Energy Mater.* **2018**, *8*, 1703173.

[37] Y. Xia, T. S. Mathis, M. Zhao, B. Anasori, A. Dang, Z. Zhou, H. Cho, Y. Gogotsi, S. Yang, *Nature* **2018**, *557*, 409.

[38] M. R. Lukatskaya, S. Kota, Z. Lin, M.-Q. Zhao, N. Shpigel, M. D. Levi, J. Halim, P.-L. Taberna, M. W. Barsoum, P. Simon, Y. Gogotsi, *Nat. Energy* **2017**, *2*, 17105.

[39] Y. Xue, P. Dai, M. Zhou, X. Wang, A. Pakdel, C. Zhang, Q. Weng, T. Takei, X. Fu, Z. I. Popov, P. B. Sorokin, C. Tang, K. Shimamura, Y. Bando, D. Golberg, *ACS Nano* **2017**, *11*, 558.

[40] H. Bi, X. Xie, K. Yin, Y. Zhou, S. Wan, L. He, F. Xu, F. Banhart, L. Sun, R. S. Ruoff, *Adv. Funct. Mater.* **2012**, *22*, 4421.

[41] J. Zhang, S. Lu, J. Li, P. Zhang, H. Xue, X. Zhao, L. Xie, *Energies* **2017**, *10*, 1.

[42] Q. Peng, J. Guo, Q. Zhang, J. Xiang, B. Liu, A. Zhou, R. Liu, Y. Tian, *J. Am. Chem. Soc.* **2014**, *136*, 4113.

[43] P. Nautiyal, L. Embrey, B. Boesl, A. Agarwal, *Carbon* **2017**, *122*, 298.

[44] J. Biener, S. Dasgupta, L. Shao, D. Wang, M. A. Worsley, A. Wittstock, J. R. I. Lee, M. M. Biener, C. A. Orme, S. O. Kucheyev, B. C. Wood, T. M. Willey, A. V. Hamza, J. Weissmüller, H. Hahn, T. F. Baumann, *Adv. Mater.* **2012**, *24*, 5083.

[45] Y. Xu, A. S. Fleischer, G. Feng, *Carbon* **2017**, *114*, 334.

[46] A. Nieto, B. Boesl, A. Agarwal, *Carbon* **2015**, *85*, 299.

[47] W. Lv, D. Tang, Y. He, C. You, Z. Shi, X. Chen, C.-M. Chen, P.-X. Hou, C. Liu, Q.-H. Yang, *ACS Nano* **2009**, *3*, 3730.